Controlling the symmetry of supercrystals formed by plasmonic core–shell nanorods with tunable cross-section

Cyrille Hamon, Claire Goldmann, Doru Constantin

Controlling the symmetry of supercrystals formed by plasmonic core-shell nanorods with tunable cross-section

Cyrille Hamon,[a*] Claire Goldmann,[a] Doru Constantin[a*]

[a]Laboratoire de Physique des Solides, CNRS, Univ. Paris-Sud, Université Paris-Saclay, 91405 Orsay Cedex, France.

E-mail : cyrille.hamon@u-psud.fr

doru.constantin@u-psud.fr

Abstract

Tailoring the crystal structure of plasmonic nanoparticle superlattices is a crucial step in controlling the collective physical response of these nanostructured materials. Various strategies can achieve this goal for isotropic nanoparticles, but few of them have been successful with anisotropic building blocks. In this work we use hybrid particles, consisting of gold nanorods encased in silver shells with a thickness that can be controlled from a few atomic layers to tens of nanometers. The particles were synthesized, characterized by a combination of techniques and assembled into supercrystals with a smectic B configuration, *i.e.* with no interlayer positional correlation. We showed that, by tuning the silver shell thickness, the in-plane order can be changed from hexagonal to square and the lattice parameters can be adjusted. The spatial distribution of the supercrystal was systematically studied by optical and electron microscopy and by small-angle X-ray scattering. Through optimized surface chemistry, we obtain homogeneous, millimeter-size films of standing nanoparticles, which hold promise for all applications using plasmon-enhanced technologies.

Keywords: gold nanorods, silver shells, heterostructures, supercrystals, self-assembly, small-angle X ray scattering, SAXS, phase transformation.

Introduction

Periodic plasmonic structures have potential applications in many research fields, such as biosensors, nanophotonics, catalysis, or light harvesting.[1] In these assemblies the nanoparticles are close together, increasing dramatically the electromagnetic fields at interparticle gaps and creating so-called hotspots.[2] Tailoring the crystal structure (lattice symmetry and interparticle distances) in order to optimize this field enhancement is a major challenge for the predictive design of new functional materials and can sometimes be achieved by covering the building blocks with a soft corona of ligands.[3] Intriguing effects were revealed for ligand lengths close to the size of the nanoparticles.[3-5] For instance, a transition from an FCC to a BCC phase and even complex Frank-Kasper phases were observed in crystals of small hydrophobic gold nanoparticles.[6-7] Another group achieved continuous symmetry variation from simple cubic to rhombohedral phases by changing the ligand excess in the solution.[8] While the "soft shell" strategy is successful for small and isotropic nanoparticles, only little success has yet been obtained with large and/or anisotropic building blocks.

Anisotropic plasmonic nanoparticles are promising candidates for applications, since they show enhanced optical properties as compared to their spherical counterparts, both in colloidal suspension and when assembled into supercystalline structures.[9-11] Gold nanorods are an emblematic example due to the tunability of their optical properties across a broad spectral range by aspect ratio variation and to their ease of synthesis.[12] Under controlled conditions, they can be assembled into hexagonal supercrystalline structures that are excellent substrates for ultrasensitive Surface Enhanced Raman Scattering (SERS) spectroscopy.[13-14] Unfortunately, owing to their larger size (typically above 10 nm), the "soft shell" approach is no longer effective in controlling the lattice symmetry. Strategies based on DNA recognition have been shown,[15-16] but still limited success in anisotropic nanoparticle-based systems has been achieved. Recently, Smalyukh and co-workers have shown an in-plane square arrangement of

gold nanorods after surface modification with Rhodamine B.[17] The interparticle distances in self-assembled structures can also be modulated using a "hard shell", e.g. by means of pre-encapsulation within silica.[18-19] However, the silica shell tends to adopt a spherical shape, leading to the loss of anisotropy[20] which hinders any preferential orientation after self-assembly. Furthermore, the presence of a dielectric material in-between the metal cores reduces the magnitude of the local electric field.

A more promising method is the hetero-epitaxial deposition of metals such as silver.[21-23] Gold nanorods have been shown to adopt a cuboidal shape upon coating with silver (AuNR-Ag),[24-26] and these particles adopt a square in-plane local organization in supercrystals as noted by Liz-Marzán and coworkers.[27] Importantly, this organization led to a dramatic enhancement of the SERS sensing property as compared to the gold nanorods supercrystal counterpart.[27] Liang and coworkers described the organization of AuNR-Ag into staircase superstructures with tunable SERS enhancement.[28] In the last two examples, the surface of the superstructures was characterized locally by electronic microscopy and the authors noted AuNR-Ag adopting either parallel or standing conformation in respect to the substrates within the same sample.

Inspired by these works, we advanced the hard-shell strategy by means of varying the silver thickness to control the crystalline structure. Although we noted a few examples reporting the self-assembly of AuNR-Ag,[27-28] such a systematic study has never been attempted. Notably, we focused on the self-assembly of AuNR-Ag with tunable thickness of the silver shell, from a few atomic layers to tens of nanometers. In addition to electronic microscopy, we used Small Angle X-Ray Scattering (SAXS) in order to reveal the 3D arrangement of the nanoparticles in the superlattices and found a clear dependence between the thickness of the silver coating and the supercrystalline phase. We also identified the critical thickness value at which changes in the lattice symmetry are observed. This study opens avenues for the predictive design of AuNR-Ag supercrystals for ultrasensitive SERS and more generally for optical devices.

Result and discussion

Synthesis and characterization of AuNR-Ag

AuNR (44.5 +/- 3.2 nm long; 14.7 +/- 1.62 nm thick) were synthesized by a seed-mediated process involving a prereduction step with salicylic acid.[29-30] In a second step, a silver shell was epitaxially grown onto the gold nanorods and its thickness was controlled by adjusting the amount of silver precursor and ascorbic acid as reducing agent in the reaction mixture.[25-26, 31] Although ascorbic acid was used under slightly acidic conditions, heating the samples up to 60 °C greatly enhanced the silver deposition rate and the overall reaction time was fixed to 3h. We studied seven samples, denoted as **1** to **7** in **Table 1** and in **Figure 1**. The experimental parameters were adjusted to optimize the colloidal synthesis and we found that even a 0.2 eq of silver to gold ratio led to complete coverage of the gold nanorods (**Figure S1**). The silver to gold ratio was systematically increased up to a value of 8, leading to important changes in the structural and optical features of the nanoparticles (**Figure 1**).

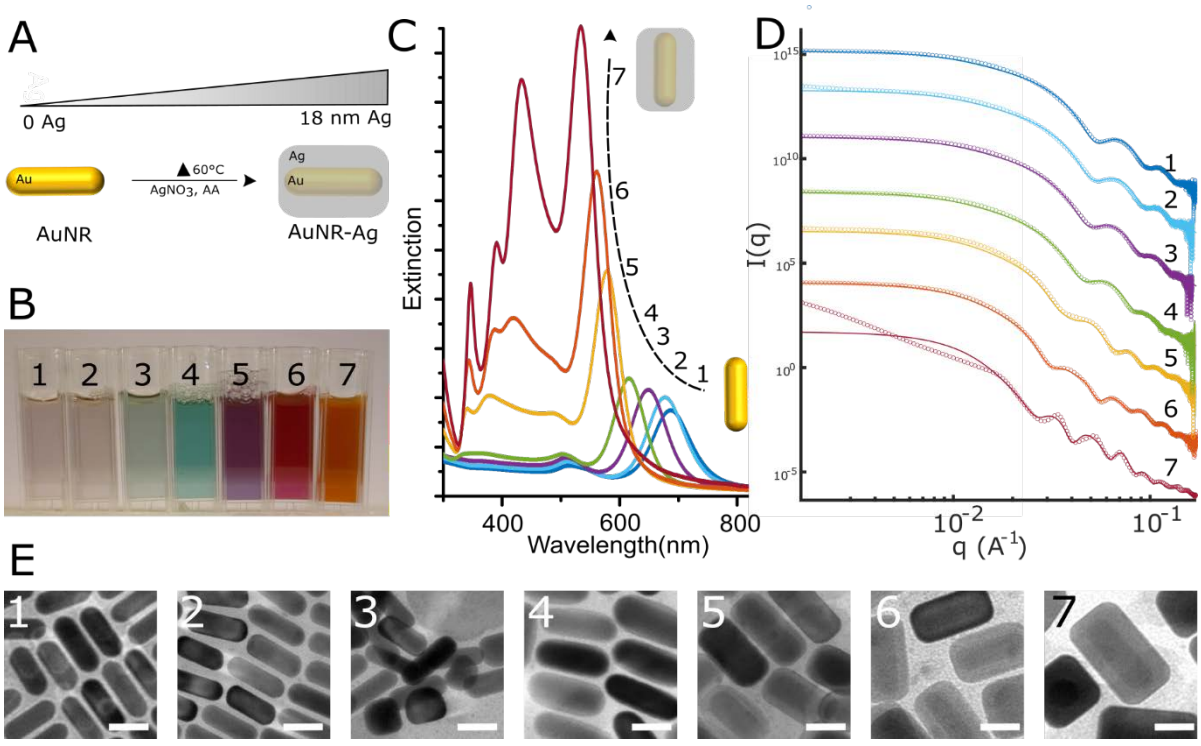

Figure 1: Colloidal design of AuNR-Ag. A) Scheme depicting the preparation of AuNR-Ag. B) Photograph of the AuNR-Ag suspensions used in this work, labelled from **1** to **7**. C)

Corresponding UV/Vis spectra and D) SAXS spectra of diluted suspension (open circles) with fits (solid lines). The curves are shifted vertically for clarity. E) Transmission Electron Microscopy images of the same AuNR-Ag. Scale bar on all images is 20 nm.

Increasingly thicker silver shells on the gold core lead to a strong color shift of the colloidal suspensions, from light brown to deep orange (**Figure 1B**). This color evolution is due to the blue shift of the longitudinal plasmon peak (related to a decrease in nanorod aspect ratio, as the silver shell grows preferentially on the lateral facets) and to the appearance of new peaks.[23,29] We modelled the optical properties by the Boundary Element Method (BEM)[32-34] and found good agreement with the experimental spectra (**Figure S2**). The initial gold nanorod suspension displayed a longitudinal dipolar mode at 698 nm and a transverse dipolar mode at 515 nm. Conversely, the thickest AuNR-Ag sample was characterized by four plasmonic peaks which can be ascribed to the longitudinal dipolar mode (at 535 nm), transverse dipolar (at 432 nm) and a combination of multipolar modes (at 388 nm and 345 nm) originating from the superposition of higher-order transverse and longitudinal modes.[31, 35-36]

The azimuthally integrated intensity I(q) is shown for all samples in **Figure 1D** as open dots and is very well described by the form factor model (see the SI for details), except for sample **7**, where the power-law increase at small q signals the formation of aggregates in solution. Particle dimensions were determined directly from the form factor models, while transmission electron microscopy (TEM) yielded independent, yet very similar estimates. The nanoparticle parameters (width W, length L and polydispersity index PDI) as obtained by the different techniques are summarized in **Table 1**.

Table 1: Dimensions of the nanoparticles determined by complementary techniques. Nanoparticle width (W) and length (L), as obtained via the three methods. In TEM, the dimensions were calculated by averaging over at least 100 particles. The polydispersity index (PDI) is calculated as the ratio between the standard deviation and the mean of the diameter multiplied by 100. In SAXS, all parameters were determined by modelling the form factor of dilute suspensions (Figure 1D).

		TEM			SAXS			BEM	
Sample label	Equivalent Ag/Au	W (nm)	L (nm)	PDI (%)	W (nm)	L (nm)	PDI (%)	W (nm)	L (nm)
1	0	14.7	44.5	11	14,6	43,7	10	14.6	42.8
2	0.2	15.6	43.5	11.75	14,6	43,7	10	15	43.0
3	0.4	16.6	44.9	11.1	14,6	44,5	10	16.2	43.6
4	0.8	17.7	44.1	10.0	16	45	10	18.1	44.6
5	2	22.8	44.0	7.2	20,5	45	7	20.8	46.0
6	4	26.4	48.6	7.8	24,0	48	6	25.6	48.5
7	8	32.5	53.7	6.3	31,0	50	4	31.6	51.6

It is noteworthy that the PDI decreases with the shell thickness, a feature readily apparent from the increased definition of the oscillations of the SAXS spectra (**Figure 1D**). The narrower range is an example of 'size-distribution focusing', which originates from the faster growth of small nanocrystals compared to larger ones; as a result, the ensemble progresses towards uniformity.[37-38] The reduction of size distribution is an important result in the view of obtaining higher-order structures with little defects.[39]

Supercrystal fabrication

A great challenge in material science is organizing anisotropic building blocks with a homogeneous orientation in order to propagate the anisotropy to the macroscopic level. We used a slow drying process in order to increase the yield of supercrystal formation.[13, 40] We functionalized the particles with two different surface ligands, cetyltrimethylammonium bromide (CTAB) and (1-mercaptoundec-11-yl)hexa(ethyleneglycol) (MUDOL). CTAB was

selected as an efficient way to generate AuNR-Ag supercrystals, as previously reported.[28] MUDOL has been reported to induce AuNR packing in a standing conformation,[41] though it has not yet been used with AuNR-Ag. These two types of ligands were grafted on sample **1** and sample **7** and corresponding supercrystals were investigated after drop casting and complete evaporation by SAXS (**Scheme 1**).

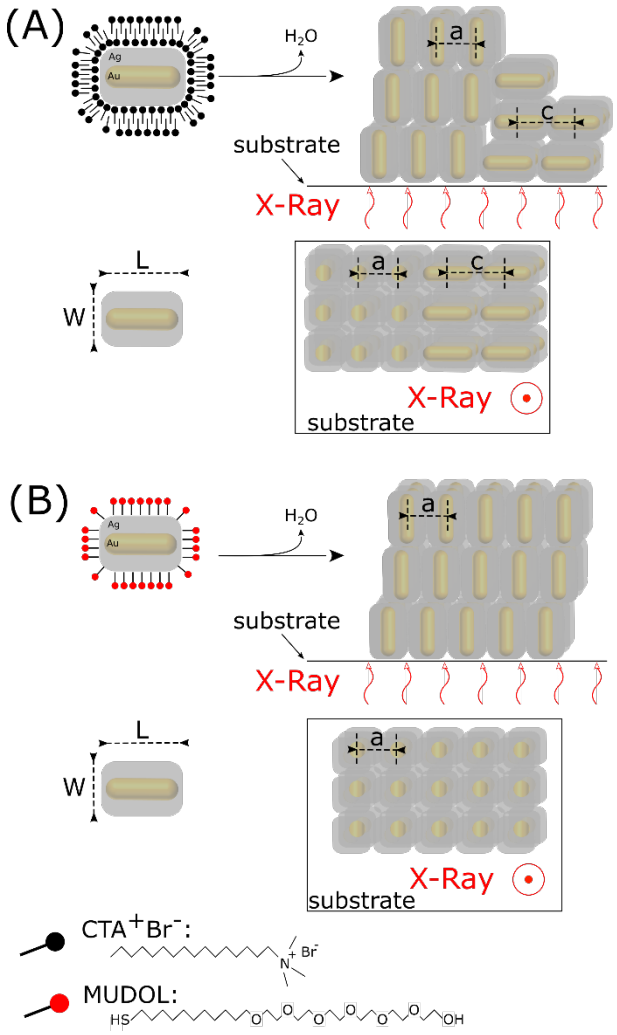

Scheme 1: **Scheme depicting the two methods for the preparation of supercrystals in this work**. **A)** AuNR-Ag perpendicular and parrallel to the substrate are observed when AuNR-Ag coated with CTAB are used to form supercrystals by slow water evaporation. **B)** After a ligand exchange step with MUDOL, the same procedure was followed and ended up with standing supperlatices of AuNR-Ag. An illustration of the side and top view is displayed for each

configuration. The lattice parameters “a” defines the core to core intralamellar distance while “c” defines the core to core interlamellar distance. The length L and width W of the AuNR-Ag are defined in the manuscript.

Under the same drying conditions, we noted substantial differences in macroscopic and local organization as a function of shell thickness (**1** *vs.* **7**) and ligand nature. MUDOL-coated nanoparticles formed homogeneous films, whereas CTAB ones resulted in coffee ring deposit,[42] suggesting two different self-assembly pathways. From previous work it is known that MUDOL-AuNR form supercrystals in solution, which are subject to sedimentation in a second step.[43] On the other hand, CTAB-AuNR are more influenced by capillary flows during evaporation.[44] We also observed differences in the deposition pattern of similarly coated CTAB nanoparticles with increasing Ag thickness. The thickest CTAB-**7** sample deposited homogenously (**Figure 2D**), while evaporation of the thinner CTAB-**4** formed a coffee ring deposit (**Figure S4**). These deposits were probed by SAXS (**Figure 2**).

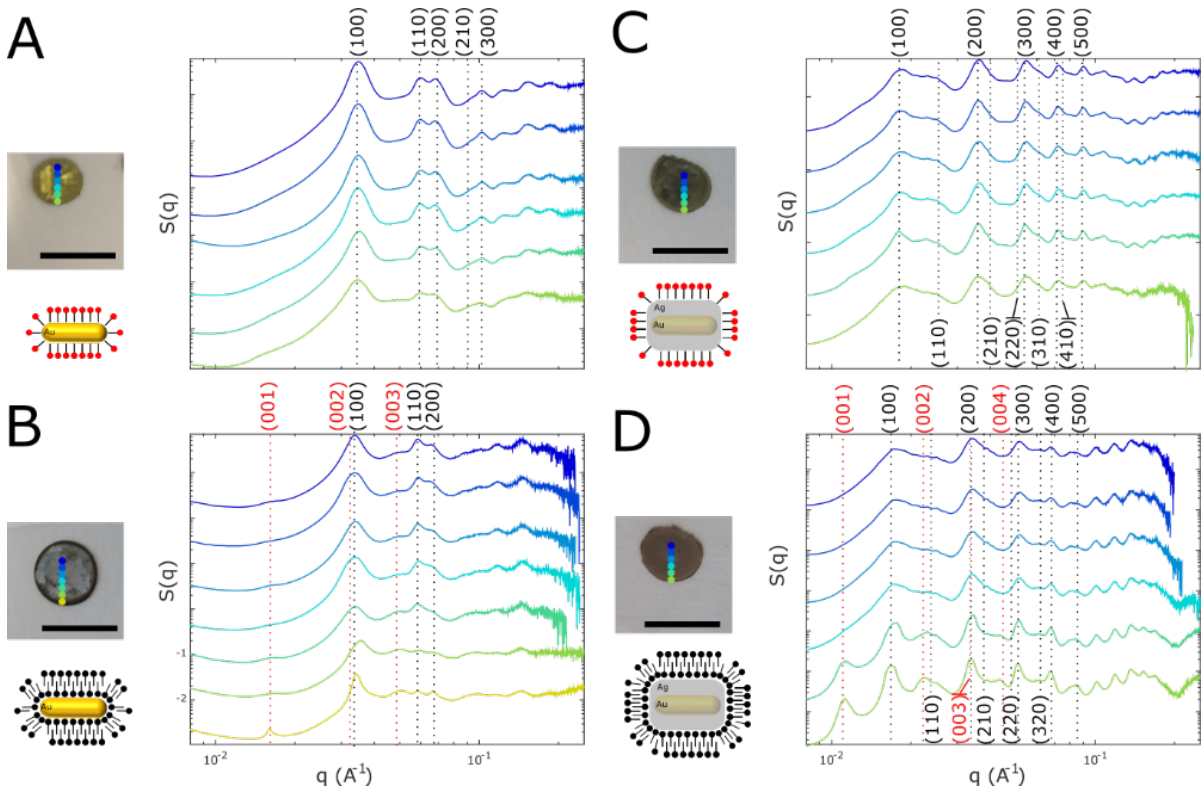

Figure 2: Spatially resolved SAXS on AuNR-Ag supercrystals thin films. A) MUDOL-**1**, **B)** CTAB-**1**, **C)** MUDOL-**7**, **D)** CTAB-**7**. Insets show photographs of the deposit, with the scale bar being 0.5 cm in all images. Beam positions corresponding to the SAXS measurement are marked on the image, with the same color code as for the SAXS curves. The drawings illustrate the nanoparticles and coating. Dotted vertical lines indicate the expected positions of the Bragg peaks, with the associated *hkℓ* indices (see text).

The thin films were mounted on a sample holder (**Figure S5**) and scanned with the SAXS beam (the beam size is 500 × 200 µm^2, in the horizontal and vertical direction, respectively) in order to retrieve the spatial distribution and organization of the nanoparticles on the substrate. The structure factor S(q) is obtained as the ratio between the corrected intensity of the supercrystal and the modelled form factor (fits in Figure 1D). The spectrum obtained from sample **1,** coated with either CTAB or MUDOL, exhibited Bragg peaks in a 1:√3:2:√7:3 progression,

characteristic of the in-plane hexagonal arrangement (with indices *h* and *k*) of standing rods (black dashed line **Figure 2A-B**). Additional lamellar organization (indexed by ℓ) was noted in the case of CTAB-**1** with a sharp peak noted within the coffee ring deposit (red dashed line **Figure 2B**). There is no correlation between the particles layers, as we can infer from the lack of "coupled" Bragg peaks (with both in-plane $h\neq0$ and interplane $\ell\neq0$ components); thus, the overall arrangement of the superlattice can be ascribed to a smectic B organization.[45] In other words, the (hexagonally ordered) monolayers are not in registry with each other, in agreement with the previous observation of moiré interferences patterns in AuNR assemblies.[46] The lattice parameters were determined to be a = 20.7 nm for MUDOL-AuNR and a = 21.3 nm, c = 44.9 nm for CTAB-AuNR. Similar experiments were carried out on the batch with the thickest Ag shell (sample **7**), for which the SAXS spectra were markedly different from the uncoated nanorods: the 1:√2:2:√5:√8 progression of the in-plane Bragg peaks (black dashed lines **Figure 2C-D**) indicates a square lattice arrangement of sample **7** assemblies. The lamellar stacking was also clear in the case of the CTAB-**7** in the outer region of the deposit (red dashed lines in **Figure 2C-D**) but, once again, the layers are not in registry. The organization in this case is also reminiscent of the smectic B type, although with square in-plane symmetry (it can also be seen as a smectic E phase with square unit cell and all equivalent objects). It is worth emphasizing that this last finding is in disagreement with previous reports[27-28] describing a tetragonal arrangement of CTAB-AuNR-Ag (with interlayer positional correlation). The lattice parameters were determined from the experimental data as: a = 35.0 nm for MUDOL-**7** and a = 37.0 nm, c = 56.0 nm for CTAB-**7**. The nanoparticles adopt a standing configuration all over the substrate, except close to the edge of the deposit when CTAB was used. Moreover, we have shown that assemblies utilizing MUDOL ligands were advantageous compared to CTAB in terms of uniformity of the standing superlattices, which span the whole deposition pattern. In the following, we only consider MUDOL coating.

Controlling the lattice symmetry in anisotropic nanoparticle superlattices is a major challenge in material science. Here, this is achieved by systematically varying the silver thickness before self-assembly into supercrystals. In each case, we investigated homogeneous thin films for samples **1** to **7** and characterized them by spatially resolved SAXS. In the following, we will compare one spectrum per sample (**Figure 3**). All data are shown in **Figure S6-S7**).

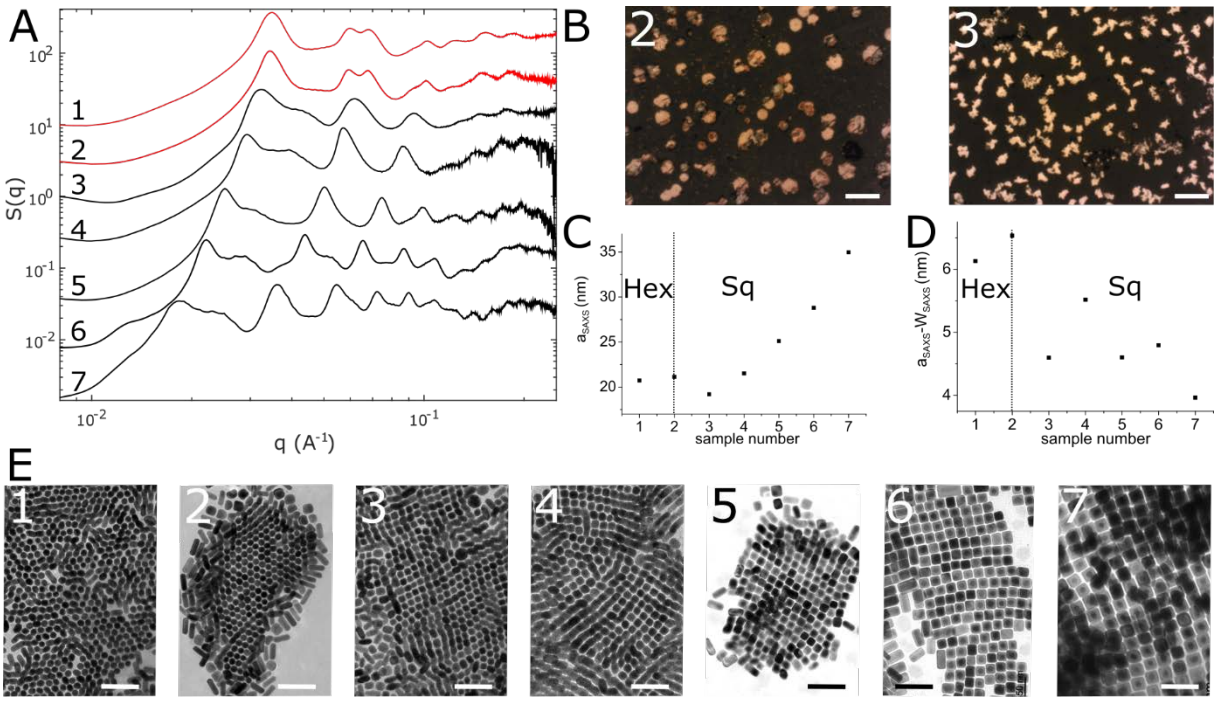

Figure 4: Determination of the critical silver thickness at which the in-plane symmetry switches from hexagonal to square. A) Structure factors of supercrystals obtained from samples **1** to **7**. The two spectra in red correspond to a hexagonal arrangement whereas the ones in black exhibit square symmetry. **B)** Optical microscopy images of two types of supercrystals obtained either from sample **2** (left) and sample **3** (right) deposited on a glass slide. Scale bar on the two images is 4 µm. **C)** Lattice parameter "a" determined from SAXS for each type of supercrystal. **D)** Interdistance a-W between nanorods. Parameters "a" and "W" (defined in **Scheme 1**) are determined by SAXS. **E)** Corresponding TEM images of the same samples, assembled into monolayers. Scale bar on all images is 100 nm.

We observed a progressive increase of the lattice parameters in supercrystals, in correlation with the thickness of the silver shells, as shown by the shift of the q_{100} peak toward smaller values (**Figure 3A**). The peaks of samples **1** and **2** were indexed to a hexagonal lattice (red curves, **Figure 3A**), in contrast with the square symmetry of samples **3** through **7** (black curves, **Figure 3A**). Importantly, we do not observe any oblique lattice in the SAXS spectra (**Figure 3A**), which would correspond to the intermediate phase between a hexagonal and an in-plane square phase. The lattice symmetry change occurs for rather thin (1.9 nm) silver shells, suggesting a significant morphological change of the nanoparticles. This is confirmed by the TEM images, in which the apparently circular initial cross-section of the rods (corresponding in fact to an octagonal shape[47]) changes markedly to a square cross-section (**Figure 3E**). The phase transformation is thus directly related to the modification of the cross-section of the particles, which then undergo shape-dependent ordering upon solvent evaporation. Moreover, the turning point in the lattice symmetry is also confirmed by Fast Fourier Transform analysis of the TEM images, which reveals sixfold symmetry for the first two samples and fourfold symmetry for the others (**Figure S8**). The symmetry change was also observed on a larger scale by optical microscopy: the supercrystals are rounded for samples **1** and **2** but become angular from sample **3** onwards (**Figure 3B**). Interdistances were determined as the difference between the lattice parameter "a" and the width of the corresponding nanoparticles measured by SAXS and a slight lattice contraction was noted after the hexagonal to square transition, *i.e.* from 6 nm to 4 nm (**Figure 3C-D**). We conducted control experiments in order to confirm these results. SAXS experiments were reproduced with suspensions dried in cylindrical capillaries. Although the drying conditions were different, we obtained similar structures (**Figure S9**). We also studied two other batches, prepared using different gold cores, and confirmed that the switch in crystal lattice symmetry occurs for very thin silver shells (**Figure S10-S11**).

We then compared the amount of silver added experimentally to the theoretical amount needed to turn a gold nanorod with regular octagonal cross-section into a square-shaped one. The latter can be estimated by subtracting the volume of the cuboidal shell by the volume of the core. Monocrystalline gold nanorods are featured with eight {250} lateral facets defining an octagonal cross section and are terminated by tips facets which are a combination of the {111} and {110} types while the silver shell adopts a cuboidal shape enclosed by six {100} facets.[24, 47] In the case of very thin shell, there is not enough silver to form a cuboid around the core and the shape of AuNR-Ag seems identical to the gold nanorod template (*i.e.* sample **1** *vs* sample **3** in **Figure 1**). However, TEM characterization of the same particles standing on the substrate, revealed that their cross section is square-shaped (**Figure 3E**). Taken together, these observations suggest a preferential deposition of silver on the {250} facets of the gold nanorods template which then evolve to a cuboid as more silver is introduced during the synthesis. The minimum amount of silver needed to square the cross section can be estimated in this configuration (see **Figure S12** and discussion therein) and correspond to the quantity added in sample **3** in which the lattice symmetry switch is observed experimentally (**Figure S14**). We checked this methodology for other gold nanorods batches and found that this rough calculation is an efficient way of predicting the lattice symmetry in AuNR-Ag supercrystals (**Figure S10-S11**).

Conclusion

In summary, we investigated AuNR-Ag supercrystals by varying systematically the silver shell thickness in order to control both the distance between the gold cores and the symmetry of the lattice. The AuNR-Ag particles were characterized in colloidal suspension and in the resulting assemblies by a combination of techniques. In particular, Small Angle X-Ray Scattering (SAXS) was methodically used to characterize their organization. After particle synthesis and functionalization, we obtained supercrystals by solvent evaporation. Two types of deposition

patterns were observed, depending on the surface chemistry of the nanorods: either coffee rings or more homogeneous films, the latter being highly oriented. Notably, this study demonstrates the suitability of the ligand MUDOL to functionalize either gold or silver surfaces to obtain supercrystalline structures. We found a clear dependence between the thickness of the silver coating and the supercrystal symmetry and we demonstrate that the hexagonal arrangement shifts to the square transition from few nanometer of silver. In each case, the supercrystals adopt a smectic B configuration, with no interlayer positional correlation. The systematic study carried in this work is of great interest to ultimately pave the way toward an optimized architecture design for the broad range of plasmonic applications.

Experimental section

Materials

All the reactants were purchased from Sigma Aldrich and used without further purification: Hexadecyltrimethylammonium bromide (CTAB, ≥99%), hexadecyltrimethylammonium chloride (CTAC, 25 wt % in H_2O), 5-bromosalicylic acid (90%), hydrogen tetrachloroaurate trihydrate ($HAuCl_4 \cdot 3H_2O$, ≥99.9%), silver nitrate ($AgNO_3$, ≥99.0%), L-ascorbic acid (AA, ≥99%), sodium borohydride ($NaBH_4$, 99%), and (1-mercaptoundec-11-yl)hexa(ethyleneglycol) (MUDOL, >90%). Water purified by reverse osmosis with a resistivity (>15 MΩ.cm) was used in all experiments.

Synthesis of gold nanorods

Gold nanorods were synthesized through a seed-mediated approach according to previously reported methods.[29-30] For the preparation of the seeds, 50 µL of a 0.025 M $HAuCl_4$ solution was added to 4.7 mL of 0.1 M CTAB solution at 30°C; after mixing, 300 µL of a freshly prepared 0.01 M $NaBH_4$ solution was injected under vigorous stirring. The growth solution was constituted with 100 mL of 0.05 M of CTAB in which 90 mg of 5-bromosalicylic acid were dissolved. Then, 960 µL of 0.01 M $AgNO_3$ and 2 mL of 0.025 M $HAuCl_4$ solution were added to the mixture. The absorbance at 396 nm was monitored in a cuvette with 1cm optical path

length until it reached 0.65, indicating suitable prereduction conditions. Then 260 µL of 0.1 M Ascorbic acid solution was added under vigorous stirring, immediately followed by 160 µL of seed solution. The mixture was left undisturbed at 30°C for at least 4 h. Gold nanorods presented an LSPR with an absorption maximum at 720 nm. The suspension was purified by 3 centrifugations (7100g, 40min) and pellet redispersion in a solution of 1 mM CTAC. AuNR suspensions were stable for months.

Silver coating

Overgrowth was performed according to recently published protocols.[24, 31] The purified AuNR were centrifuged at 8500g for 30 min and redispersed in a 10 mM CTAC solution at a final gold concentration of 0.25 mM in all samples. The silver-to-gold molar ratio was adjusted as described in Table 1. The molar ratio between the Ag precursor and AA was fixed to 4 in all experiments. After mixing, the reaction vials were kept at 60 °C during 3h to yield AuNR-Ag. After the synthesis, particles were purified from the excess of reactant by two centrifugation steps (7100g, 40min) and pellet redispersion in a solution of 1 mM CTAB at a final gold concentration of 0.25 mM in all samples.

Surface modification with MUDOL and preparation of the supercrystals

For MUDOL grafting, 10 µL of 10 mM MUDOL solution were added to 10mL of the purified CTAB-AuNR-Ag (0.25mM Au, 1mM CTAB) and left to incubate for 24h. The resulting MUDOL AuNR-Ag were then directly used to form supercrystals by droplet evaporation. For SAXS experiments, the nanoparticles were first concentrated by centrifugation to a gold concentration of 16 mM. Then, 10 µL of AuNR-Ag was cast on a glass coverslip and dried in a homemade apparatus[13]; complete evaporation was observed after 12h. Alternatively, 60 µL of MUDOL AuNR-Ag was inserted in capillaries and dried under vaccum; complete evaporation was observed after more than 24h. A similar procedure was adopted for TEM experiments (TEM JEOL 1400, 120kV) albeit with a lower gold concentration (1.5 mM), to

yield preferentially monolayers on the grid (Ted Pella, 300 mesh Cu). Experiments with CTAB-AuNR-Ag were carried out similarly, skipping the surface modification step.

SAXS Experiments

The SAXS data was collected at the SWING beamline of the SOLEIL synchrotron (Saint-Aubin, France), at a beam energy of 12 keV and two sample-to-detector distances (1.42 and 6.52 m). The samples were contained in cylindrical glass capillaries (Mark-Rörchen, Germany) of calibrated diameter, placed in a motorized and temperature-controlled holder. The scattered signal was recorded by an Eiger 4M detector (Dectris Ltd., Switzerland) with pixel size 75 µm. Preliminary data treatment (angular averaging and normalization) was done using the software Foxtrot developed at the beamline and yielded the intensity as a function of the scattering vector I(q) in absolute units. Subsequent data modelling was done in Igor Pro using some models available in the NCNR SANS package[48] and others developed in-house (see the Supporting Information for more details).

Acknowledgment:

The present work has benefited from the electronic microscopy facility of Imagerie-Gif, (http://www.i2bc.paris-saclay.fr), member of IBiSA (http://www.ibisa.net), supported by "France-BioImaging" (ANR-10-INBS-04-01), and the Labex "Saclay Plant Science" (ANR-11-IDEX-0003-02). We acknowledge SOLEIL for the provision of synchrotron radiation facilities and we thank Javier Pérez for assistance in using beamline SWING.

References

1. Dreaden, E. C.; Alkilany, A. M.; Huang, X.; Murphy, C. J.; El-Sayed, M. A., The golden age: gold nanoparticles for biomedicine. *Chemical Society Reviews* **2012,** *41* (7), 2740-2779.
2. Halas, N. J.; Lal, S.; Chang, W.-S.; Link, S.; Nordlander, P., Plasmons in Strongly Coupled Metallic Nanostructures. *Chemical Reviews* **2011,** *111* (6), 3913-3961.
3. Boles, M. A.; Engel, M.; Talapin, D. V., Self-Assembly of Colloidal Nanocrystals: From Intricate Structures to Functional Materials. *Chemical Reviews* **2016,** *116* (18), 11220-11289.

4. Gang, O.; Zhang, Y., Shaping Phases by Phasing Shapes. *ACS Nano* **2011,** *5* (11), 8459-8465.
5. Silvera Batista, C. A.; Larson, R. G.; Kotov, N. A., Nonadditivity of nanoparticle interactions. *Science* **2015,** *350* (6257).
6. Hajiw, S.; Pansu, B.; Sadoc, J.-F., Evidence for a C14 Frank–Kasper Phase in One-Size Gold Nanoparticle Superlattices. *ACS Nano* **2015,** *9* (8), 8116-8121.
7. Schmitt, J.; Hajiw, S.; Lecchi, A.; Degrouard, J.; Salonen, A.; Impéror-Clerc, M.; Pansu, B., Formation of Superlattices of Gold Nanoparticles Using Ostwald Ripening in Emulsions: Transition from fcc to bcc Structure. *The Journal of Physical Chemistry B* **2016,** *120* (25), 5759-5766.
8. Zhang, Y.; Lu, F.; van der Lelie, D.; Gang, O., Continuous Phase Transformation in Nanocube Assemblies. *Physical Review Letters* **2011,** *107* (13), 135701.
9. Reguera, J.; Langer, J.; Jimenez de Aberasturi, D.; Liz-Marzan, L. M., Anisotropic metal nanoparticles for surface enhanced Raman scattering. *Chemical Society Reviews* **2017**.
10. Li, N.; Zhao, P.; Astruc, D., Anisotropic Gold Nanoparticles: Synthesis, Properties, Applications, and Toxicity. *Angewandte Chemie International Edition* **2014,** *53* (7), 1756-1789.
11. Baffou, G.; Quidant, R., Nanoplasmonics for chemistry. *Chemical Society Reviews* **2014,** *43* (11), 3898-3907.
12. Chen, H.; Shao, L.; Li, Q.; Wang, J., Gold nanorods and their plasmonic properties. *Chemical Society Reviews* **2013,** *42* (7), 2679-2724.
13. Scarabelli, L.; Hamon, C.; Liz-Marzán, L. M., Design and Fabrication of Plasmonic Nanomaterials Based on Gold Nanorod Supercrystals. *Chemistry of Materials* **2017,** *29* (1), 15-25.
14. Bodelon, G.; Montes-Garcia, V.; Lopez-Puente, V.; Hill, E. H.; Hamon, C.; Sanz-Ortiz, M. N.; Rodal-Cedeira, S.; Costas, C.; Celiksoy, S.; Perez-Juste, I.; Scarabelli, L.; La Porta, A.; Perez-Juste, J.; Pastoriza-Santos, I.; Liz-Marzan, L. M., Detection and imaging of quorum sensing in Pseudomonas aeruginosa biofilm communities by surface-enhanced resonance Raman scattering. *Nat Mater* **2016,** *15* (11), 1203-1211.
15. Jones, M. R.; Macfarlane, R. J.; Lee, B.; Zhang, J.; Young, K. L.; Senesi, A. J.; Mirkin, C. A., DNA-nanoparticle superlattices formed from anisotropic building blocks. *Nat Mater* **2010,** *9* (11), 913-917.
16. Macfarlane, R. J.; Lee, B.; Jones, M. R.; Harris, N.; Schatz, G. C.; Mirkin, C. A., Nanoparticle Superlattice Engineering with DNA. *Science* **2011,** *334* (6053), 204-208.
17. Liang, Y.; Xie, Y.; Chen, D.; Guo, C.; Hou, S.; Wen, T.; Yang, F.; Deng, K.; Wu, X.; Smalyukh, I. I.; Liu, Q., Symmetry control of nanorod superlattice driven by a governing force. *Nature Communications* **2017,** *8* (1), 1410.
18. Lu, Y.; Yin, Y.; Li, Z.-Y.; Xia, Y., Synthesis and Self-Assembly of Au@SiO2 Core−Shell Colloids. *Nano Letters* **2002,** *2* (7), 785-788.
19. Correa-Duarte, M. A.; Sobal, N.; Liz-Marzán, L. M.; Giersig, M., Linear Assemblies of Silica-Coated Gold Nanoparticles Using Carbon Nanotubes as Templates. *Advanced Materials* **2004,** *16* (23-24), 2179-2184.
20. Sanz-Ortiz, M. N.; Sentosun, K.; Bals, S.; Liz-Marzán, L. M., Templated Growth of Surface Enhanced Raman Scattering-Active Branched Gold Nanoparticles within Radial Mesoporous Silica Shells. *ACS Nano* **2015,** *9* (10), 10489-10497.
21. Gu, J.; Zhang, Y.-W.; Tao, F., Shape control of bimetallic nanocatalysts through well-designed colloidal chemistry approaches. *Chemical Society Reviews* **2012,** *41* (24), 8050-8065.

22. Xia, Y.; Xiong, Y.; Lim, B.; Skrabalak, S. E., Shape-Controlled Synthesis of Metal Nanocrystals: Simple Chemistry Meets Complex Physics? *Angewandte Chemie International Edition* **2009,** *48* (1), 60-103.
23. Guo, P.; Sikdar, D.; Huang, X.; Si, K. J.; Xiong, W.; Gong, S.; Yap, L. W.; Premaratne, M.; Cheng, W., Plasmonic core-shell nanoparticles for SERS detection of the pesticide thiram: size- and shape-dependent Raman enhancement. *Nanoscale* **2015,** *7* (7), 2862-2868.
24. Gómez-Graña, S.; Goris, B.; Altantzis, T.; Fernández-López, C.; Carbó-Argibay, E.; Guerrero-Martínez, A.; Almora-Barrios, N.; López, N.; Pastoriza-Santos, I.; Pérez-Juste, J.; Bals, S.; Van Tendeloo, G.; Liz-Marzán, L. M., Au@Ag Nanoparticles: Halides Stabilize {100} Facets. *The Journal of Physical Chemistry Letters* **2013,** *4* (13), 2209-2216.
25. Park, K.; Drummy, L. F.; Vaia, R. A., Ag shell morphology on Au nanorod core: role of Ag precursor complex. *Journal of Materials Chemistry* **2011,** *21* (39), 15608-15618.
26. Okuno, Y.; Nishioka, K.; Kiya, A.; Nakashima, N.; Ishibashi, A.; Niidome, Y., Uniform and controllable preparation of Au-Ag core-shell nanorods using anisotropic silver shell formation on gold nanorods. *Nanoscale* **2010,** *2* (8), 1489-1493.
27. Gómez-Graña, S.; Pérez-Juste, J.; Alvarez-Puebla, R. A.; Guerrero-Martínez, A.; Liz-Marzán, L. M., Self-Assembly of Au@Ag Nanorods Mediated by Gemini Surfactants for Highly Efficient SERS-Active Supercrystals. *Advanced Optical Materials* **2013,** *1* (7), 477-481.
28. Yang, X.; Li, J.; Zhao, Y.; Yang, J.; Zhou, L.; Dai, Z.; Guo, X.; Mu, S.; Liu, Q.; Jiang, C.; Sun, M.; Wang, J.; Liang, W., Self-assembly of Au@Ag core-shell nanocuboids into staircase superstructures by droplet evaporation. *Nanoscale* **2018,** *10* (1), 142-149.
29. Scarabelli, L.; Grzelczak, M.; Liz-Marzán, L. M., Tuning Gold Nanorod Synthesis through Prereduction with Salicylic Acid. *Chemistry of Materials* **2013,** *25* (21), 4232-4238.
30. Ye, X.; Jin, L.; Caglayan, H.; Chen, J.; Xing, G.; Zheng, C.; Doan-Nguyen, V.; Kang, Y.; Engheta, N.; Kagan, C. R.; Murray, C. B., An Improved Size-Tunable Synthesis of Monodisperse Gold Nanorods through the Use of Aromatic Additives. *ACS Nano* **2012**.
31. Tebbe, M.; Kuttner, C.; Mayer, M.; Maennel, M.; Pazos-Perez, N.; König, T. A. F.; Fery, A., Silver-Overgrowth-Induced Changes in Intrinsic Optical Properties of Gold Nanorods: From Noninvasive Monitoring of Growth Kinetics to Tailoring Internal Mirror Charges. *The Journal of Physical Chemistry C* **2015,** *119* (17), 9513-9523.
32. Hohenester, U.; Trügler, A., MNPBEM – A Matlab toolbox for the simulation of plasmonic nanoparticles. *Computer Physics Communications* **2012,** *183* (2), 370-381.
33. García de Abajo, F. J.; Howie, A., Retarded field calculation of electron energy loss in inhomogeneous dielectrics. *Physical Review B* **2002,** *65* (11), 115418.
34. Myroshnychenko, V.; Rodriguez-Fernandez, J.; Pastoriza-Santos, I.; Funston, A. M.; Novo, C.; Mulvaney, P.; Liz-Marzan, L. M.; Garcia de Abajo, F. J., Modelling the optical response of gold nanoparticles. *Chemical Society Reviews* **2008,** *37* (9), 1792-1805.
35. Jiang, R.; Chen, H.; Shao, L.; Li, Q.; Wang, J., Unraveling the Evolution and Nature of the Plasmons in (Au Core)–(Ag Shell) Nanorods. *Advanced Materials* **2012,** *24* (35), OP200-OP207.
36. Cortie, M. B.; Liu, F.; Arnold, M. D.; Niidome, Y., Multimode Resonances in Silver Nanocuboids. *Langmuir* **2012,** *28* (24), 9103-9112.
37. Reiss, H., The Growth of Uniform Colloidal Dispersions. *The Journal of Chemical Physics* **1951,** *19* (4), 482-487.
38. Yin, Y.; Alivisatos, A. P., Colloidal nanocrystal synthesis and the organic–inorganic interface. *Nature* **2004,** *437*, 664.

39. O'Brien, M. N.; Jones, M. R.; Mirkin, C. A., The nature and implications of uniformity in the hierarchical organization of nanomaterials. *Proceedings of the National Academy of Sciences* **2016,** *113* (42), 11717-11725.
40. Ming, T.; Kou, X.; Chen, H.; Wang, T.; Tam, H.-L.; Cheah, K.-W.; Chen, J.-Y.; Wang, J., Ordered Gold Nanostructure Assemblies Formed By Droplet Evaporation. *Angewandte Chemie* **2008,** *120* (50), 9831-9836.
41. Xie, Y.; Guo, S.; Ji, Y.; Guo, C.; Liu, X.; Chen, Z.; Wu, X.; Liu, Q., Self-Assembly of Gold Nanorods into Symmetric Superlattices Directed by OH-Terminated Hexa(ethylene glycol) Alkanethiol. *Langmuir* **2011,** *27* (18), 11394-11400.
42. Deegan, R. D.; Bakajin, O.; Dupont, T. F.; Huber, G.; Nagel, S. R.; Witten, T. A., Capillary flow as the cause of ring stains from dried liquid drops. *Nature* **1997,** *389* (6653), 827-829.
43. Hamon, C.; Sanz-Ortiz, M. N.; Modin, E.; Hill, E. H.; Scarabelli, L.; Chuvilin, A.; Liz-Marzan, L. M., Hierarchical organization and molecular diffusion in gold nanorod/silica supercrystal nanocomposites. *Nanoscale* **2016,** *8* (15), 7914-7922.
44. Hamon, C.; Henriksen-Lacey, M.; La Porta, A.; Rosique, M.; Langer, J.; Scarabelli, L.; Montes, A. B. S.; González-Rubio, G.; de Pancorbo, M. M.; Liz-Marzán, L. M.; Basabe-Desmonts, L., Tunable Nanoparticle and Cell Assembly Using Combined Self-Powered Microfluidics and Microcontact Printing. *Advanced Functional Materials* **2016,** *26* (44), 8053-8061.
45. Hamon, C.; Postic, M.; Mazari, E.; Bizien, T.; Dupuis, C.; Even-Hernandez, P.; Jimenez, A.; Courbin, L.; Gosse, C.; Artzner, F.; Marchi-Artzner, V., Three-Dimensional Self-Assembling of Gold Nanorods with Controlled Macroscopic Shape and Local Smectic B Order. *ACS Nano* **2012,** *6* (5), 4137-4146.
46. Hamon, C.; Novikov, S. M.; Scarabelli, L.; Solís, D. M.; Altantzis, T.; Bals, S.; Taboada, J. M.; Obelleiro, F.; Liz-Marzán, L. M., Collective Plasmonic Properties in Few-Layer Gold Nanorod Supercrystals. *ACS Photonics* **2015,** *2* (10), 1482-1488.
47. Carbó-Argibay, E.; Rodríguez-González, B.; Gómez-Graña, S.; Guerrero-Martínez, A.; Pastoriza-Santos, I.; Pérez-Juste, J.; Liz-Marzán, L. M., The Crystalline Structure of Gold Nanorods Revisited: Evidence for Higher-Index Lateral Facets. *Angewandte Chemie* **2010,** *122* (49), 9587-9590.
48. Kline, S., Reduction and analysis of SANS and USANS data using IGOR Pro. *Journal of Applied Crystallography* **2006,** *39* (6), 895-900.